Portland State University

PDXScholar

Dissertations and Theses

Dissertations and Theses

6-4-2022

A Three-Dimensional, Analytical Wind Turbine Wake Model: Flow Acceleration, Empirical Correlations, and Continuity

Zein Ahmad Sadek
Portland State University

Follow this and additional works at: https://pdxscholar.library.pdx.edu/open_access_etds

 Part of the Aerodynamics and Fluid Mechanics Commons

Let us know how access to this document benefits you.

Recommended Citation

Sadek, Zein Ahmad, "A Three-Dimensional, Analytical Wind Turbine Wake Model: Flow Acceleration, Empirical Correlations, and Continuity" (2022). *Dissertations and Theses.* Paper 6027.
https://doi.org/10.15760/etd.7898

This Thesis is brought to you for free and open access. It has been accepted for inclusion in Dissertations and Theses by an authorized administrator of PDXScholar. Please contact us if we can make this document more accessible: pdxscholar@pdx.edu.

A Three-Dimensional, Analytical Wind Turbine Wake Model:

Flow Acceleration, Empirical Correlations, and Continuity

by

Zein Ahmad Sadek

A thesis submitted in partial fulfillment of the
requirements for the degree of

Master of Science
in
Mechanical Engineering

Thesis Committee:
Raúl Bayoán Cal, Chair
Gerald Recktenwald
Derek Tretheway

Portland State University
2022

Abstract

A new, three-dimensional, analytical, steady state wake model is presented which includes local flow acceleration near the rotor improving wake description compared to existing models. Wake structures such as the momentum deficit and regions of accelerated flow are concisely described with compound and normal Gaussian functions. Large-eddy simulations (LES) are used as training data to develop the model using two, inline turbines under various inflow conditions parameterized by hub height wind speed and turbulence intensity. Mass conservation is considered by fixing two components of the wake velocity model and optimizing the third to best satisfy continuity; after which, the model performs comparably if not better than existing work with regards to both relative error and mass consistency. The final model demonstrates a high degree of flexibility making use of empirical correlations to scale across different inflow conditions. This work will be transitioned into the open source, flow redirection and induction in steady state (FLORIS) wind farm modeling toolbox where it will be used to predict wake velocities in wind plant optimization processes. The inclusion of these effects is capable of revealing unutilized opportunities for enhanced power generation by aligning wake trajectories with these regions of accelerated flow.

Acknowledgements

I would like to first thank my advisor Raúl Bayoán Cal for his guidance, passion, and patience throughout my time spent with him. I am also thankful to my mentors Nicholas Hamilton who has greatly influenced my development as a scientist, Ryan Scott for his encouragement, as well as the Wind Energy and Turbulence lab for their collective knowledge and energetic atmosphere. This work would not have been possible without the backing, encouragement, and unrelenting enthusiasm supplied by my family.

Contents

List of Tables

List of Figures

Chapter 1

Introduction and Motivation

With the increasing effects of climate change, the push to adopt renewable energy sources is heightened [34]. Global temperatures have increased nearly 0.85°C since 1880 while sea levels have risen more than 100 mm over just the past three decades, seen in Fig. 1.1. These worldwide effects pose great threats to both the environment and global markets. Renewable energies have been popularized as efforts are made to phase out fossil fuels. These zero emission alternatives make use of natural resources to generate clean energy [38]. Different resources have advantages and disadvantages corresponding to their abundance, energy content, method of collection, and other factors. Of the these renewable energies, wind power has recently seen large investments and a reduction in the cost per generated power [1]. The availability of this resource has also been well characterized through multiyear averages of wind speed measurements.

Fig. 1.2 shows the average wind speeds across the Unites States at 100 m above the ground. There are many regions where the natural topography of the terrain is conducive to generating favorable wind patterns; an example of which spans the eastern portion of the Rocky mountain range [19]. Further measurements reveal an increase in wind speed with gains in elevation, due to the interactions between

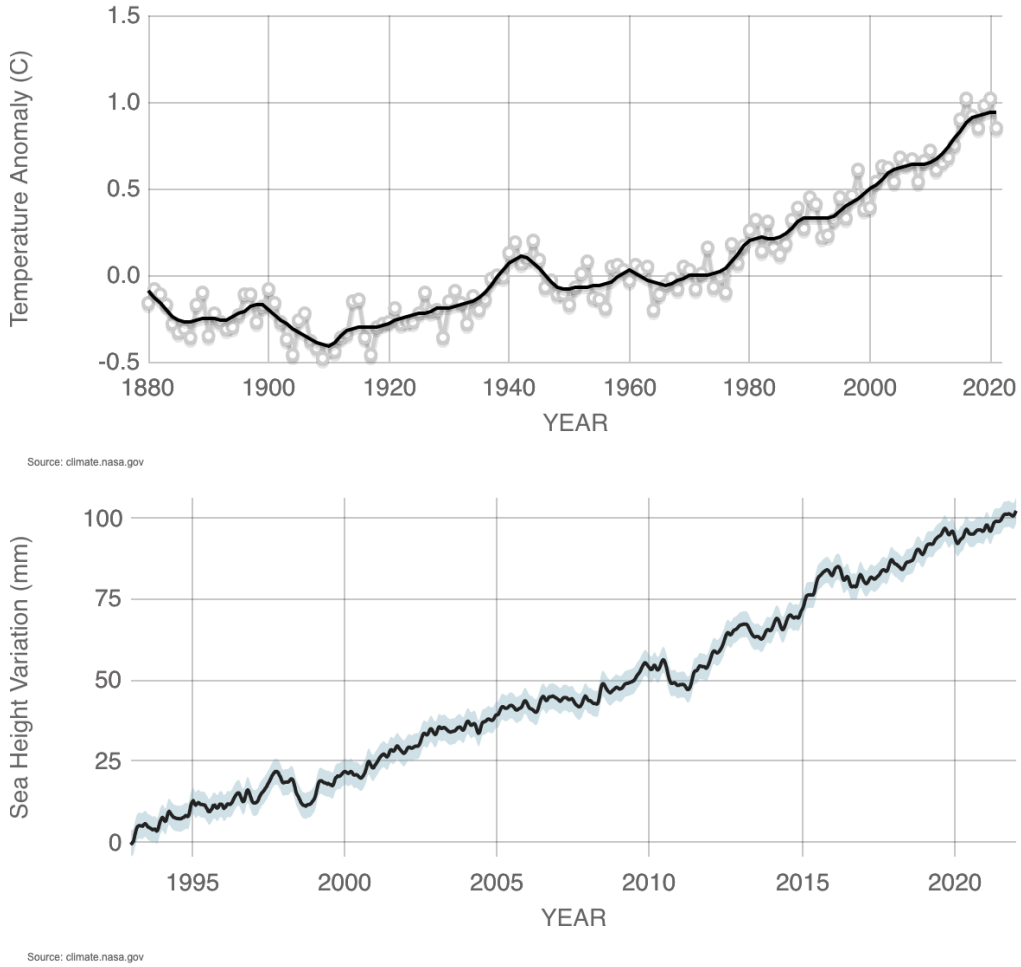

Figure 1.1: Top: Change in global surface temperature compared to average temperatures between 1951 and 1980 [2]. **Bottom:** Rise in sea level relative to measurements made in 1993, via satellite imagery [3].

the ground and atmospheric boundary layer [15]. The distribution of this resource forces the technology used to harvest it to adapt favoring taller, larger devices.

There are many variations of technologies which exploit the wind resource yet they all act upon the simple premise of extracting kinetic energy from the flow. This is done by using the wind to rotate a shaft connected to a generator which in turn produces power. An assortment of different blade designs and configurations are

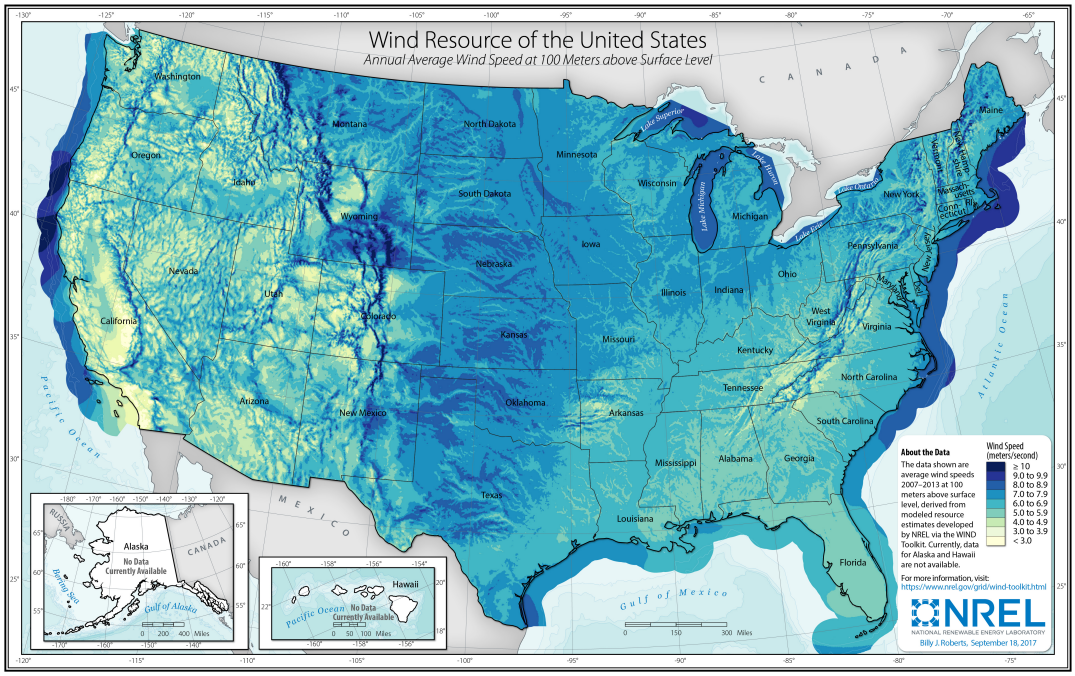

Figure 1.2: Average wind speed at 100 m above surface level across the United States (US), measured between 2007 and 2013. Chart taken from NREL [11].

used to translate the kinetic energy from the flow into a torque on the shaft [35]. Throughout the development of wind energy sciences a three bladed, horizontal axis wind turbine (HAWT) has become the best suited design for large scale applications [7]. This comes from a number of factors, the largest being performance, mechanical loading, cost of production, and scalability. A three bladed design was achieved through a balance between the economics of manufacturing blades and an increase in design complexity [29]. Installation of wind energy does come with a large overhead cost [12], however, paired with their performance and efficiency they are best used in large numbers requiring tremendous investments to develop [8]. As these machines grow in size and begin operating in relatively close proximity, the effects on their

surroundings becomes significantly important.

Wind energy development has grown significantly, with the power capacity of turbines increasing 284% over the past two decades paired with the coupled growth in adjacent technologies this trend seeks to continue [43]. In 2020, nearly 17 GW of new wind energy capacity was added to the United States (US) electrical infrastructure with a cumulative contribution of 122 GW across all installed wind plants [43]. With its large overhead costs, impressive energy potential, and enormous growth, the need for forecasting tools has risen in order to best design these wind farms and optimize their power productions.

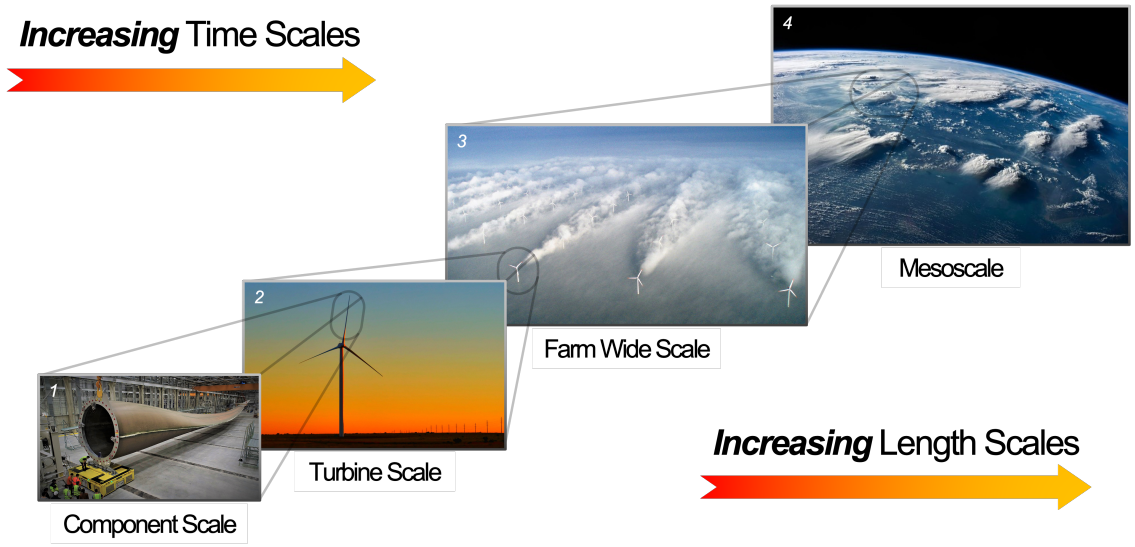

Figure 1.3: Depiction of the various length and times scales seen in wind energy. Mesoscale weather structures supply the resource. Wind farm flows include interactions between turbines and the atmospheric boundary layer. The single turbine length scale involves understanding the generated wake as its individual components interact with the flow at the smallest relevant scale. From left to right photographs are taken from: [17], [39], [40], [42].

These models exist at varying scales and fidelity. Fig. 1.3 shows the degree of length scales seen in wind energy applications, spanning the large mesoscale,

meteorological flows which dictate the behavior of this resource, down to the flow past the turbine blades. The relevance of each is dictated by which characteristic of the wind plant is being considered. Large scale meteorologic models are used to asses the wind energy potential of a location, typically used to determine the efficacy of a proposed wind plant [13]. Component scale modeling is used in the design of turbines blades and other aerodynamic features. This scale experiences the greatest overlap between fluid mechanics and solid mechanics; where material selection affects the longevity of a turbine whilst influencing its performance [27].

The length scales of greatest interest lie between the individual turbine and the full wind farm. Kinetic energy extracted from the flow results in a reduction in wind speed behind the turbine. Defined as wakes, these momentum deficient regions decrease the incident velocity seen by downstream turbines reducing their power generation [41]. Wind turbine generated wakes are among the greatest source of losses in wind plant operations [25]. Power estimates are sensitive to wind speed, driving the need for accurate wake velocity models [16].

Similar to the range of length scales found in wind energy, there are a variety of modeling techniques available, each with differing degrees of fidelity, Fig. 1.4. Shown are direct numerical simulations (DNS), large-eddy simulations (LES), and engineering models. The fidelity and complexity of these techniques varies greatly with DNS solving the full Navier-Stokes equations while engineering models are simply analytic approximations based on correlations. However, each method has merit and ties back into the discussed length scales. The complexity of DNS limits its use to the smallest scales, such as modeling the flow past individual blade segments [30]. LES is a mid-tier fidelity technique which truncates and neglects the smallest length

scales. Its balance between fidelity and complexity makes it an efficient tool for wind farm modeling and a practical substitute for field measurements [14]. Engineering models are low fidelity, analytical, time-averaged predictions developed to estimate wind turbine wake flows using empirical correlations. These simple models are used to obtain quick and applicable results in the wind plant design process [5]. Packages like the flow redirection and induction in steady state (FLORIS) toolbox are used to generate and perform wind farm optimization using these models [33]. FLORIS is an open source wake modeling resource used in controls oriented design and is maintained by the National Renewable Energy Laboratory (NREL).

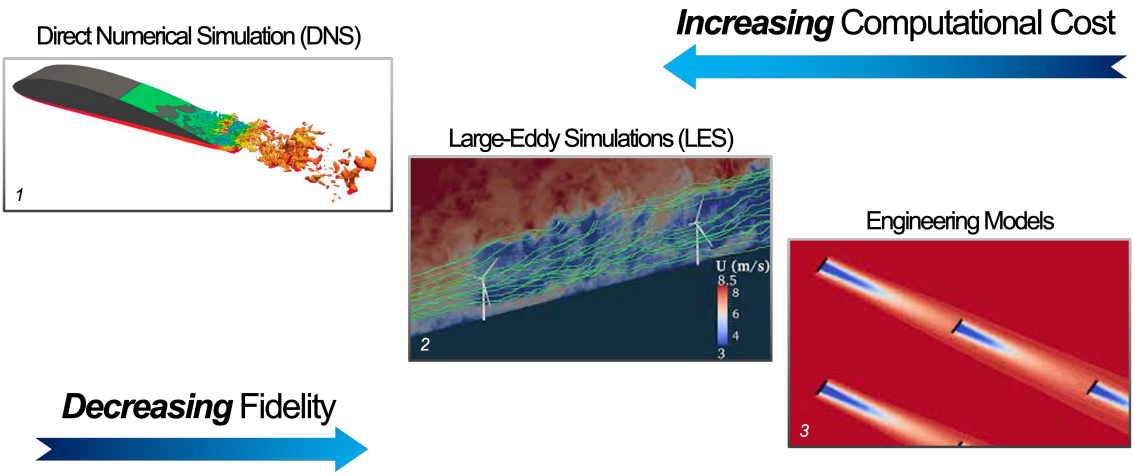

Figure 1.4: Description of different flow modeling techniques of varying fidelity and computational complexity. Shown are direct numerical simulations (DNS), large-eddy simulations (LES), and engineering models, decreasing in both fidelity and computational cost. From left to right photographs are taken from: [30], [14], [5].

These tools are needed to support the suite of engineering processes in wind plant design, optimization, and control [9]. Existing models are proven to be reliable in the far wake but typically do not accurately describe the distinctive physics in the near

wake where flow is accelerated through induction by the turbine rotor [44]. These effects are important to capture as regions of increased velocity become favorable during wind plant design. Integration of these effects is essential if the objective is to best describe the flow field. The design of horizontal axis wind turbines favors the streamwise velocity, leading to an abundance of streamwise yet lack of spanwise and vertical wake models. This results in the need for a near wake focused, three-dimensional wake model to better represent wake flows and aid in the development and optimization of wind plants.

An early wake model poses the momentum deficit as a uniform, top-hat profile whose magnitude is defined to conserve mass, as seen in Jensen [21]. Linear wake expansion is introduced, becoming canon in future models. The assumption of a uniform wake velocity is an idealization of wake behavior yet its simplicity has secured its continued use in industry [36]. New models have since been developed, introducing a Gaussian wake profile as shown in Bastankhah *et al.* [4]. This distribution better represents the time-averaged momentum deficit by diffusing the wake into the surrounding flow. This profile is an appropriate representation of the self-similar far wake but is not suitable to depict flows near the turbine. Variations of a Gaussian profile are introduced to better describe the near wake. The super-Gaussian, as introduced by Blondel and Cathelain [6], is a parameterized Gaussian function which can vary the breadth of its profile; broadening the distribution in the near wake creating a top-hat profile and transitioning to a normal Gaussian downstream. Other models describe the near wake by modifying the amplitude function of the Gaussian profile as done in Ishihara and Qian [20]. A summary for the performance of the discussed models in wind farm validation has been conducted by Hamilton *et*

al. [18].

More current models take to describing the near wake by varying the shape function, keeping with a Gaussian base. A radially displaced Gaussian profile is introduced by Keane [23], revolving about the wake center to depict accelerated flow about the turbine hub. This displacement approaches zero as the wake progresses downstream converging upon a normal Gaussian profile. Most recent is work by Soesanto *et al.* [37] who further expands double-Gaussian wake models by accounting for anisotropic wake expansion. Spanwise and vertical wake velocity models are also important but are not as well studied since the streamwise velocity contains the majority of the available kinetic energy. The currently accepted spanwise and vertical velocity model is introduced by King [24] and was developed to describe the flow fields of yaw-misaligned turbines. This again presents the need for spanwise and vertical wake velocity models dedicated to non-misaligned turbines.

Current models attempt to describe flows near the turbine using assumptions only valid in the far wake. Obstructions generated by the turbine rotor induces flow acceleration through less constricted regions; this being through the hub (hub jet) and rotor circumference (tip acceleration) [41]. A non-uniform distribution of thrust along the blades channels flow through these regions generating a local acceleration in wake velocity. These effects have been observed in previous work, where under relatively low turbulence can penetrate a considerable distance into the wake [10].

This work details the development of a mass-consistent, three dimensional model for onshore, horizontal axis wind turbines that better describes near wake flows compared to existing work by introducing a novel wake profile. LES is used to train the model through a suite of optimization process; developing empirical relations

which express the model parameters as functions of local turbulence intensity and thrust coefficient. The resultant model is to be used in the design of wind farm layout, control algorithms, and power predictions.

Inclusion of local accelerated flow is a significant feature when optimizing wind plant layout as these regions become favorable to intersect along the wake trajectory. Neglecting these effects could lead to a suboptimal wind plant design, generating less power than it otherwise could be. The theory and definitions of the streamwise, spanwise, and vertical velocity models are described in their concurrent subsections within chapter 2. Specifications regarding the LES and training data are discussed in chapter 3. Chapter 4 details the wake modeling techniques and methodology. Results regarding the performance of each model, in addition to mass consistency, is found in chapter 5 with the conclusion and future work followed in chapters 6 and 7.

Chapter 2

Theory

2.1 Streamwise Velocity

From here the suite of models being introduced will be referred to as the Sadek model. The streamwise component of the proposed model is defined in a velocity deficit sense and subsequently transformed into absolute velocities, given by

$$\hat{u} = \frac{u_\infty - u}{u_\infty}, \tag{2.1}$$

where $\hat{u}$ is the normalized velocity deficit and u_∞, u are the inflow and wake velocities, respectively. This can be interpreted as the percentage reduction in wake velocity relative to the inflow. The proposed shape function uses a primary Gaussian curve is used to generate the main momentum deficit while the compound and secondary Gaussian are used to describe flow acceleration.

$$\hat{u} = A_{\mathrm{MW}} \left(e^{-\left(\frac{r}{2\sigma_{\mathrm{MW}}}\right)^2} \right) - A_{\mathrm{TA}} \left(\left(\frac{r}{\sigma_{\mathrm{MW}}} \right)^2 e^{-\left(\frac{r}{2\sigma_{\mathrm{MW}}}\right)^2} \right) - A_{\mathrm{HJ}} \left(e^{-\left(\frac{r}{2\sigma_{\mathrm{HJ}}}\right)^2} \right). \tag{2.2}$$

Equation 2.2 is the formulation for the streamwise velocity deficit model. The

coordinate system used places x, y, z in the streamwise, spanwise, and vertical directions, respectively with the origin is placed at the ground, aligned with the tower, Fig. 2.1. Being a radially symmetric model, $r = \sqrt{y^2 + (z - H)^2}$ is the distance from the wake center where H is the turbine hub height. The wake center line is fixed at the hub height as wake meandering is neglected in this work. This shape function uses five model values: three amplitudes and two widths.

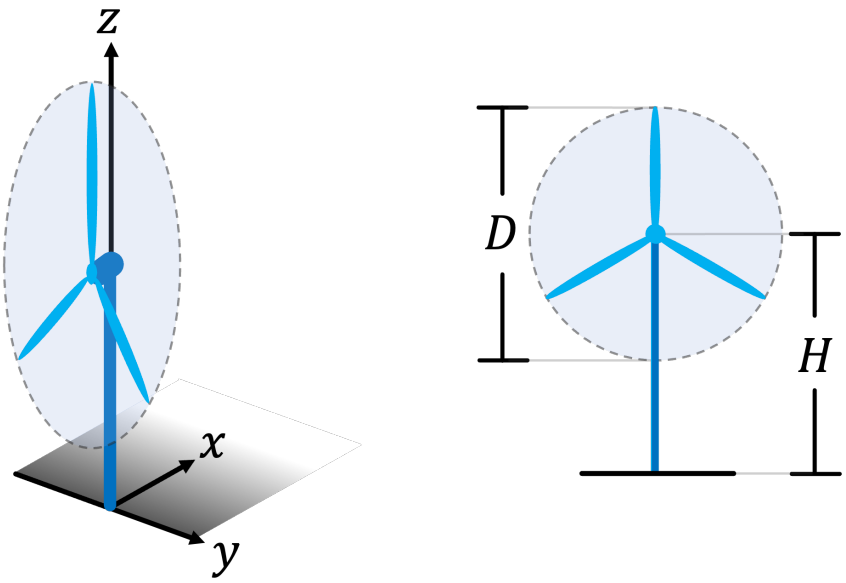

Figure 2.1: Schematic of the coordinate system used and characteristic turbine lengths. **Left:** Isometric view of turbine depicting the Cartesian coordinate system used. **Right:** Frontal view of turbine indicating the dimensions of rotor diameter (D) and hub height (H).

Subscripts MW, HJ and TA are used to denote model components, corresponding to 'Main Wake', 'Hub Jet', and 'Tip Acceleration', respectively. To capture the wake morphology as it evolves downstream, each model value is defined as a function of downstream position. The main wake half-width σ_{MW} and hub jet half-width σ_{HJ} are defined as linear functions of downstream position, consistent with existing models.

$$\sigma_{\mathrm{MW}}(\tilde{x}) = D\left(k_{\mathrm{MW}}\tilde{x} + \varepsilon_{\mathrm{MW}}\right). \tag{2.3}$$

$$\sigma_{\mathrm{HJ}}(\tilde{x}) = D\left(\varepsilon_{\mathrm{HJ}}\right). \tag{2.4}$$

In this definition all length scales are normalized by the turbine rotor diameter D, where $\tilde{x} = x/D$, wake growth rate k, and initial size ε are expressed as dimensionless quantities.

$$A(\tilde{x}) = \left(a + b\tilde{x} + c(1+\tilde{x})^{-2}\right)^{-2}. \tag{2.5}$$

Three amplitudes are used in this model, taking the form of equation 2.5, developed by Ishihara and Qian [20] and based off work by Bastankhah *et al.* [4]. This formulation was designed to describe near wake behavior and features a sudden rise and fall in the velocity deficit magnitude. Both the main wake and hub jet amplitudes ($A_{\mathrm{MW}}, A_{\mathrm{HJ}}$) take this form where each component has unique coefficients a, b, c, used to tune the wake behavior.

$$A_{\mathrm{MW}}(\tilde{x}) = \left(a_{\mathrm{MW}} + b_{\mathrm{MW}}\tilde{x} + c_{\mathrm{MW}}(1+\tilde{x})^{-2}\right)^{-2}. \tag{2.6}$$

$$A_{\mathrm{HJ}}(\tilde{x}) = \left(a_{\mathrm{HJ}} + b_{\mathrm{HJ}}\tilde{x} + c_{\mathrm{HJ}}(1+\tilde{x})^{-2}\right)^{-2}. \tag{2.7}$$

$$A_{\mathrm{TA}}(\tilde{x}) = a_{\mathrm{TA}}e^{(-b_{\mathrm{TA}}\tilde{x})}. \tag{2.8}$$

Introducing these parameters increases the model performance yet introduces difficulty when balancing model flexibility to complexity. This is justified as this function

better describes the momentum deficit near the turbine, aligning with the aim of this work. Since tip acceleration occurs at the rotor plane and diminishes downstream, its amplitude is modeled by an exponentially decaying function, Equation 2.8. Here $a_{\mathrm{TA}}, b_{\mathrm{TA}}$, denote the maximum reduction in velocity deficit and decay rate, respectively. Tip acceleration contributes the least compared to the other components. Despite its lesser contribution it is still a phenomena which is not included in other models and may affect farm design processes since it acts on the outer most portion of the wake.

Wake superposition becomes significant when modeling multiple turbines. Existing models use a sum of squares combination model, forcing a positive definite velocity deficit. The Sadek model uses linear superposition to maintain its flow acceleration features. Induction effects accompany the physical presence of a turbine which acts as an obstruction, reducing the upstream wind speed. This work neglects these upstream flows by artificially masking the wake ahead to the rotor for each turbine. Ground flows are modeled after the no-slip condition by applying a mirror condition. This is done by inverting the vertical axis and sign of the model, then summing with the original flow field. Applying this about the ground ($z = 0$) forces zero velocity, maintaining the no-slip condition [26].

2.2 Spanwise and Vertical Velocities

The spanwise and vertical components are described as absolute velocities given the lack of a suitable reference velocity for a deficit definition. These components share similar wake structures and are described using variations of the same shape function. Both profiles display dipole-like behavior with distinct regions (nodes) of

positive and negative velocity. The behavior of these nodes lead to a clear distinction between the near and far wake. The near wake is dominated by bulk rotation induced by the motion of the rotor. This region has the nodes configured 90° out of alignment from their final position, rotating counter-clockwise as they evolve downstream.

In the far wake, the node orientation becomes independent of downstream location leaving the amplitudes to decay until the wake has fully recovered. The far wake is modeled by two equally sized, Gaussian distributions of equal and opposite amplitudes. The nodes are aligned vertically and horizontally for the spanwise and vertical velocity models, respectively. These nodes are radially offset from the wake center by $D/4$. The widths are set to a constant value given their negligible growth and the amplitudes are modeled as exponentially decaying functions of downstream position.

$$A_{\text{far}} = C_{\text{far}} e^{-\beta_{\text{far}}(\tilde{x})}. \tag{2.9}$$

$$\sigma_{\text{far}} = D\left(\mu_{\text{far}}\right). \tag{2.10}$$

$$v_{\text{far}} = w_{\text{far}} = A_{\text{far}} \left(e^{-\left(\frac{r_{\text{pos}}}{\sigma_{\text{far}}}\right)^2} - e^{-\left(\frac{r_{\text{neg}}}{\sigma_{\text{far}}}\right)^2} \right). \tag{2.11}$$

Equation 2.11 is the governing shape function for the far wake component of the spanwise and vertical velocity models, where equations 2.9, 2.10 represent the node amplitude and node width, respectively. The maximum velocity C_{far} occurs at the rotor and decays at a rate, β_{far}. The node width μ_{far} is expressed in terms of rotor diameter. The difference between the two formulations are the definitions of r_{pos} and r_{neg} which position the nodes in space.

$$r_{v,\text{pos}} = \sqrt{y^2 + (z - (D/4) - H)^2}. \tag{2.12}$$

$$r_{v,\text{neg}} = \sqrt{y^2 + (z + (D/4) - H)^2}. \tag{2.13}$$

$$r_{w,\text{pos}} = \sqrt{(y + (D/4))^2 + (z - H)^2}. \tag{2.14}$$

$$r_{w,\text{neg}} = \sqrt{(y - (D/4))^2 + (z - H)^2}. \tag{2.15}$$

To capture the interaction between the near and far wake components, the far wake model is subtracted from the training data, leaving the near wake contribution. This is modeled with a compound Gaussian function containing either a spanwise or vertical dependence, producing distinct positive and negative distributions which when combined with the far wake model capture near wake rotation.

$$A_{\text{near}} = \left(a_{\text{near}} + b_{\text{near}}\tilde{x} + c_{\text{near}}(1 + \tilde{x})^{-2}\right)^{-2}. \tag{2.16}$$

$$\sigma_{\text{near}} = D\left(\alpha_{\text{near}}\tilde{x} + \mu_{\text{near}}\right). \tag{2.17}$$

$$v_{\text{near}} = A_{\text{near}}(y)\left(\frac{r}{\sigma_{\text{near}}}\right)^2 e^{-\left(\frac{r}{\sigma_{\text{near}}}\right)^2}. \tag{2.18}$$

Shown above are the general formulations for the near wake component of the spanwise and vertical velocity models. Parameters are distinguished by subscripts (v, near) and (w, near) corresponding to the spanwise and vertical components respectively. The amplitude function shown in equation 2.16 adopts the Ishihara formulations with terms $a_{\text{near}}, b_{\text{near}}, c_{\text{near}}$ used to capture induction upstream of the rotor while the width develops linearly with growth rate, α_{near}, and initial width,

μ_{near}, Equation 2.17.

Equation 2.18 is the complete, near wake contribution for the spanwise model with the vertical sharing a similar formulation. The flow field is created by linearly superimposing the near and far wake components: $v = v_{\text{near}} + v_{\text{far}}$ and $w = w_{\text{near}} + w_{\text{far}}$. Equations 2.19, 2.20 are the full expressions for the spanwise and vertical velocity models.

$$v = A_{v,\text{near}}(y)\left(\frac{r}{\sigma_{v,\text{near}}}\right)^2\left(e^{-\left(\frac{r}{\sigma_{v,\text{near}}}\right)^2}\right) + A_{v,\text{far}}\left(e^{-\left(\frac{r_{v,\text{pos}}}{\sigma_{v,\text{far}}}\right)^2} - e^{-\left(\frac{r_{v,\text{neg}}}{\sigma_{v,\text{far}}}\right)^2}\right). \tag{2.19}$$

$$w = A_{w,\text{near}}(z-H)\left(\frac{r}{\sigma_{w,\text{near}}}\right)^2\left(e^{-\left(\frac{r}{\sigma_{w,\text{near}}}\right)^2}\right) + A_{w,\text{far}}\left(e^{-\left(\frac{r_{w,\text{pos}}}{\sigma_{w,\text{far}}}\right)^2} - e^{-\left(\frac{r_{w,\text{neg}}}{\sigma_{w,\text{far}}}\right)^2}\right). \tag{2.20}$$

Similar to the streamwise model, the spanwise and vertical wakes are linearly superimposed and a mirror condition is applied. The vertical velocity model does not include any prescribed inflow as it contains no coherent structures. However, the spanwise inflow is significant and is modeled as a function of the incident veer and streamwise inflow. Wind veer $\phi(y, z)$ is defined as the angle misalignment in wind direction from the streamwise direction.

$$\phi(y,z) = -\tan^{-1}(v_\infty, u_\infty). \tag{2.21}$$

$$\Delta\phi = \phi\left(0, H + D/2\right) - \phi\left(0, H - D/2\right). \tag{2.22}$$

$$\tau = \Delta\phi\left(\frac{z-H}{D}\right). \tag{2.23}$$

$$v_{\infty,\text{model}} = u_\infty \tan\left(-\tau\right). \tag{2.24}$$

This is calculated using equation 2.21 by taking the inverse tangent between the spanwise v_∞ and streamwise u_∞ inflows. The sign is inverted to align the veer quantity with the spanwise coordinate. A difference in veer is found across the rotor diameter (Equation 2.22) and used to generate a vertically varying, linear model seen in Equation 2.23. The spanwise inflow is constructed by solving Equation 2.21 for v_∞ while substituting in the newly solved linear veer model, resulting in Equation 2.24.

Chapter 3

Simulation Setup

Models are developed using a suite of large-eddy simulations provided by the National Renewable Energy Laboratory (NREL) conducted using the Simulator for On/Offshore Wind Farm Applications (SOWFA) framework. The SOWFA framework is a high-fidelity simulator for wind turbine dynamics used to test and implement new controls strategies. All simulations contain the NREL 5 MW reference turbine with a rotor diameter of $D = 126\,\mathrm{m}$ and hub height of $H = 90\,\mathrm{m}$ [22]. The simulation domain is $4\,\mathrm{km} \times 1\,\mathrm{km} \times 0.3\,\mathrm{km}$ in the streamwise, spanwise, and vertical dimensions, respectively with 10 m resolution in all dimensions. A precursor simulation was run for 20,000 seconds to generate turbulent inflow. The turbines are then placed in the domain where time averaged statistics are recorded for the next 1,700 seconds. Note that a 300 second delay is used between the placement of the turbines and collection of data. The data set used is comprised of eight different simulations featuring identical farm layouts with two 5 MW turbines placed inline, $10D$ downstream from each other.

A smaller domain is used during analysis to focus on the wake and remove superfluous background flow, indicated by white dashed lines in Fig. 3.1. By using two turbines, the number of values used to develop empirical relations is doubled

while also expanding the range of operating conditions considered by forcing higher turbulence intensities onto the trailing turbines.

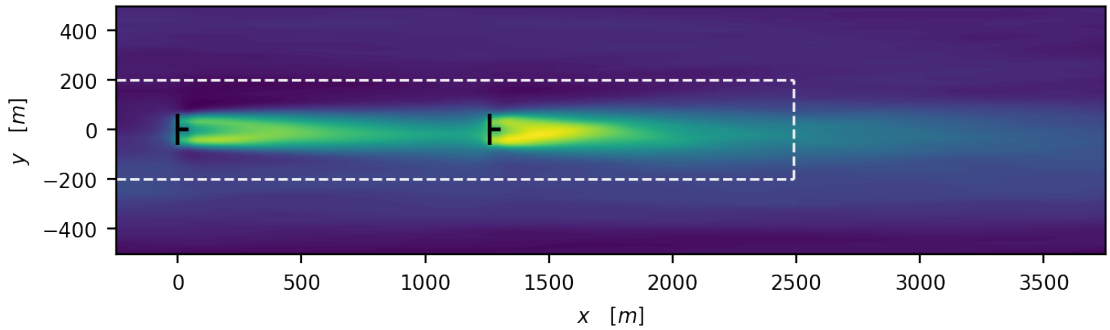

Figure 3.1: Hub height, horizontal contour through full LES domain. Region used during analysis is outlined by the dashed white lines. Two NREL 5 MW turbines are placed inline with a downstream spacing of 10 rotor diameters (1260 m).

Shown in Fig. 3.2 is the distribution of thrust C_t and power C_p coefficients for each turbine in the data set. The dashed line is the characteristic curve for both quantities of the 5 MW turbine, which are functions of incident wind speed. Values are determined by taking the rotor averaged wind velocity $1D$ upstream of the turbine and referencing the respective characteristic curve. Sampling at this distance supplies the representative wind speed experienced by the turbine by avoiding the effects of both induction and the previous turbine's wake.

Table 3.1 is a breakdown of the flow conditions for each simulation. Included are the case names, mean inflow velocity, and local turbulence intensities and thrust coefficients for each turbine. Local turbulence intensities are obtained from the LES. Ambient turbulence intensity is modified by altering the surface roughness of the simulation domain with low intensity cases prescribed a surface roughness of 0.0002 m and high intensity 0.15 m.

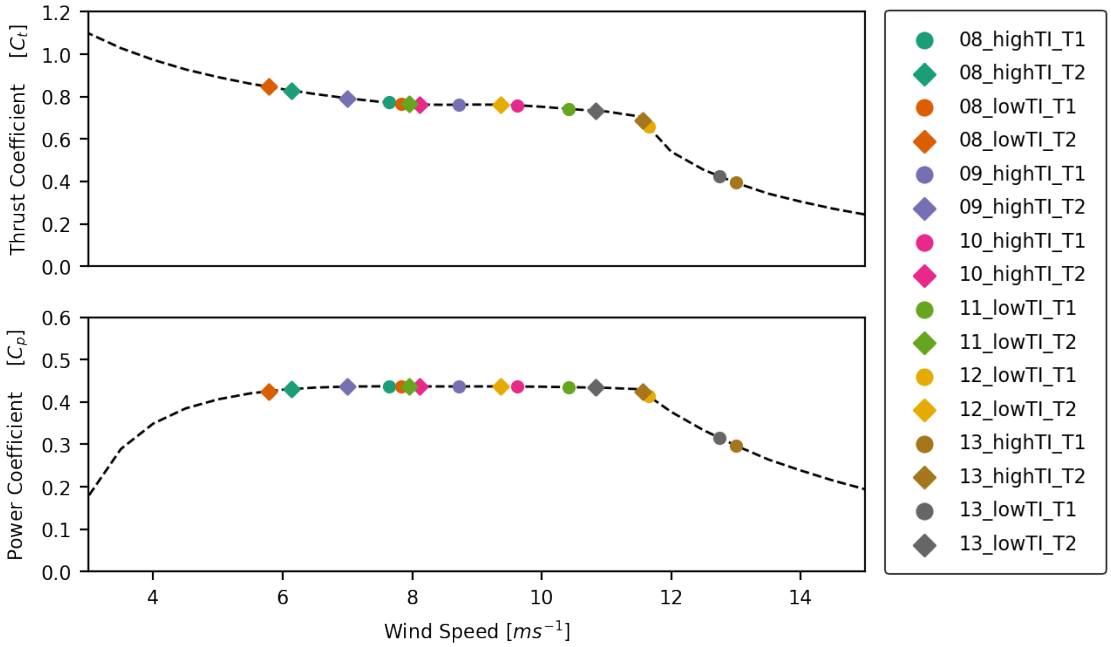

Figure 3.2: Distribution of thrust (Top) and power coefficients (Bottom) for each turbine across all simulations. Leading turbines and following turbines are denoted by circles and diamonds, respectively, sharing the same infill color across different cases. The black dashed lines are the characteristic thrust and power curves for the NREL 5 MW turbine.

		Turbine 1		**Turbine 2**	
Case	Inflow $[m/s]$	C_t	Ti	C_t	Ti
08_highTI	8	0.0928	0.7723	0.1289	0.8290
08_lowTI	8	0.0665	0.7673	0.0973	0.8467
09_highTI	9	0.1226	0.7620	0.1834	0.7922
10_highTI	10	0.1812	0.7593	0.1766	0.7626
11_lowTI	11	0.0605	0.7423	0.1053	0.7641
12_lowTI	12	0.0081	0.6572b	0.1402	0.7619
13_highTI	13	0.0158	0.3938	0.0844	0.6869
13_lowTI	13	0.0027	0.4254	0.0445	0.7334

Table 3.1: Table with a summary of specifications for each simulation used in analysis. This includes the case name, average inflow wind speed, and local turbulence intensity and thrust coefficient for each turbine in the array. Turbine 1 is leading while turbine 2 is trailing.

Chapter 4

Wake Modeling

In order to maximize the utility of the model a suite of optimization methods are used to generate best fit, empirical relations. Dependence is placed on local turbulence intensity and thrust coefficient. This is applied to every model parameter by introducing three empirical values, shown by

$$\kappa = C_0 Ti^{C_1} {C_t}^{C_2}. \tag{4.1}$$

Equation 1.1 is a formulation developed by Ishihara and Qian [20] to describe a model parameter κ as a function of local turbulence intensity Ti and thrust coefficient C_t. This uses a coefficient C_0, turbulence intensity exponent C_1, and thrust coefficient exponent C_2; all of which are determined through optimization operations. Dual dependence on turbulence intensity and thrust coefficient gives the model greater tuning abilities by considering both the ambient flow conditions and turbine operational state. While this definition creates a more flexible model, the total parameter space explodes three-fold since each single parameter requires three empirical values. It is to be noted that the main wake growth rate k_{MW} is modeled as a linear function of turbulence intensity,

$$k_{\mathrm{MW}} = C_0 Ti + C_1, \tag{4.2}$$

consistent with Niayifar and Porté-Agel [31].

To assist the optimization process, an initial empirical model set it first created. Constructing the streamwise model a Downstream Marching Algorithm (DMA) is used which passes through each spanwise-vertical crossplane in the data set and fits a Gaussian profile at each instance. Initial statistics are derived by using this process, determining values for the wake amplitude and widths of each model component. Each value is then fit with their defining function, shown in Fig. 4.1. Wake superposition is taken into account by processing the leading turbine and extrapolating the modeled parameters, then subtracting this from the wake of the following turbine. This is repeated for each case in the data set. Parameters derived from fitting are plotted as functions of local turbulence intensity and thrust coefficient for each turbine and used to produce an initial empirical model using Equation 1.1. The downstream marching algorithm is favorable since the independence between crossplanes best depicts the behavior of each model value as the wake progresses downstream.

A large scale minimization scheme is used to consider all cases simultaneously, where the target value being minimized is

$$\zeta = \left(\sum_{n=1}^{N} \eta_n^2 \right)^{1/2}, \tag{4.3}$$

where ζ is the sum of squares of the individual domain-wide, L^2 norm errors given by

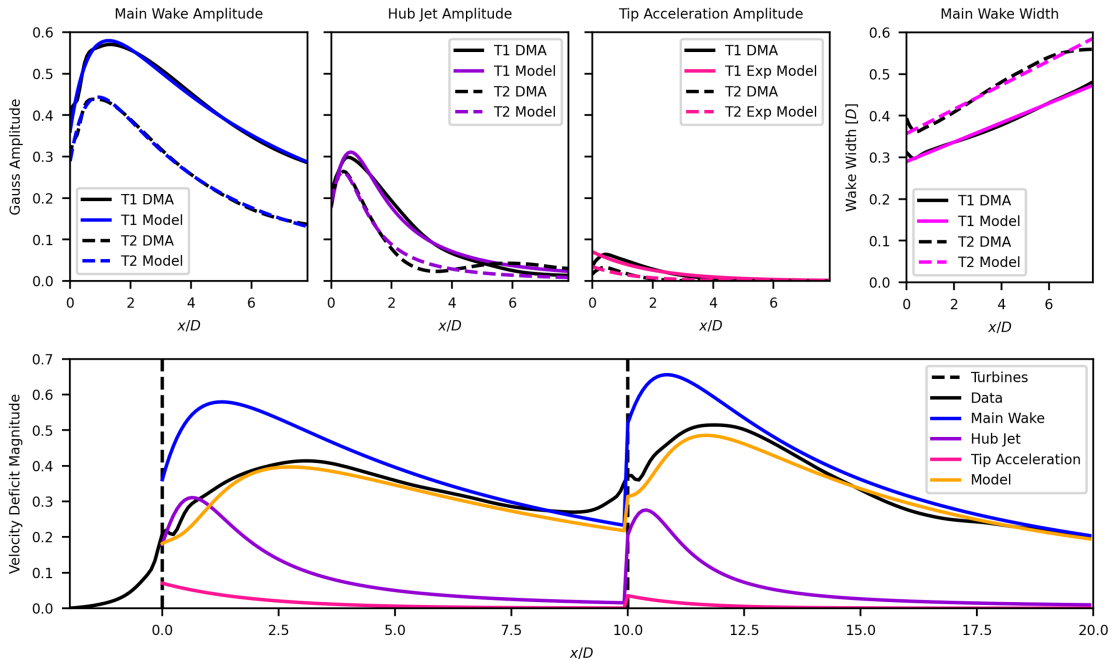

Figure 4.1: Demonstration of the downstream marching algorithm (DMA) for a single case. **Top:** Wake amplitudes and growth rate for both turbines plotted against normalized downstream position. Leading turbine quantities are shown in solid lines while the trailing turbine is dashed. Black values are the result from DMA and the colored curves are from corresponding fits. **Bottom:** Superposition of wake amplitudes to generate a prediction for the wake center line velocity deficit.

$$\eta = \frac{||\text{Data} - \text{Model}||}{||\text{Data}||}. \tag{4.4}$$

Double vertical bars indicate the L^2 norm of an array. Equation 4.3 takes the sum of squares of the domain-wide errors across a data set of size N, where in this work $N = 8$. This optimization uses the quasi-Newton method of Broyden, Fletcher, Goldfarb, and Shanno (BFGS) as the minimization algorithm [32].

To apply this minimization in a computationally feasible manner different com-

ponents of the model are optimized while constraining the rest. This is first applied to the main wake component while all other parameters are fixed. The empirical values needed to describe the three amplitude parameters $a_{\mathrm{MW}}, b_{\mathrm{MW}}, b_{\mathrm{MW}}$ and main wake width growth rate k_{MW} are left to be optimized. The initial main wake ϵ_{MW} and hub jet widths ϵ_{HJ} are left as constant values which do not vary as a function of ambient and operational conditions. Defining constant values aids in reducing the model parameter space; becoming a thirteen degree-of-freedom optimization.

Comparing the errors between the main wake optimized model to the initial inputs shows the process produced beneficial results, reducing error across all cases. The process of optimizing and comparing is repeated for the remaining wake components until the final streamwise model is achieved. Given the smaller parameter space of the spanwise and vertical models, only large scale minimization is considered. Initial values are derived by independently optimizing each case rather than using DMA. The optimized parameters from each case are again plotted against the ambient conditions for each turbine and used to generate initial inputs for the larger process.

Applying conservation principles can only be done by considering all three models simultaneously. Mass conservation for an incompressible flow is expressed by the continuity equation

$$\frac{\partial u}{\partial x} + \frac{\partial v}{\partial y} + \frac{\partial w}{\partial z} = \gamma, \tag{4.5}$$

where in an entirely mass consistent system $\gamma = 0$. While difficult to achieve with analytic models, the objective instead becomes reducing the remaining residuals γ to approach zero. Tuning all parameters within the Sadek suite would prove to be

computationally intensive and risk forfeiting the performance of each model. To avoid this, only one of the three models is left to be optimized while the remaining were fixed. This reduces the computational power required yet grants a considerable portion of the parameter space to the minimization process. The vertical component is chosen to be the tuning basis while the streamwise and spanwise are fixed. This process again considers all cases in the data set, where the target objective ζ is instead the sum of squares of the L^2 norm of residuals generated in each case, given by

$$\zeta = \left(\sum_{n=1}^{N} ||\gamma_n||^2 \right)^{1/2} . \tag{4.6}$$

This preserves prior work in developing the fixed models and shuttles all the variability into the less utilized velocity model. Absolute mass conservation is not guaranteed but model flexibility is utilized to acknowledge conservation principles.

Chapter 5

Results

5.1 Streamwise Model

Comparisons are drawn between the Sadek, Bastankhah, Ishihara, Blondel, and Jensen wake models for each case in the data set. The domain-wide L^2 norm, relative error is used as a comparative metric to judge model performance. Local turbulence intensities are provided for each turbine across all models, eliminating the use of auxiliary turbulence models and solely examines the capabilities of the wake velocity models. The dependence of thrust coefficient on incident wind speed leads to variation based on the employed model; this is left to vary and is determined within FLORIS. Corresponding combination methods are used with the Sadek model linearly superimposing its wakes while the remaining use a sum of squares combination model. Equivalent inflow profiles are provided for each flow field.

Figure 5.1 shows the domain-wide, L^2 norm error of each streamwise FLORIS model across the training data set. Generally all models are performing well, operating under 10% error. However, for every case the Sadek model out performs all existing models with the lowest computed error. This demonstrates its adaptability

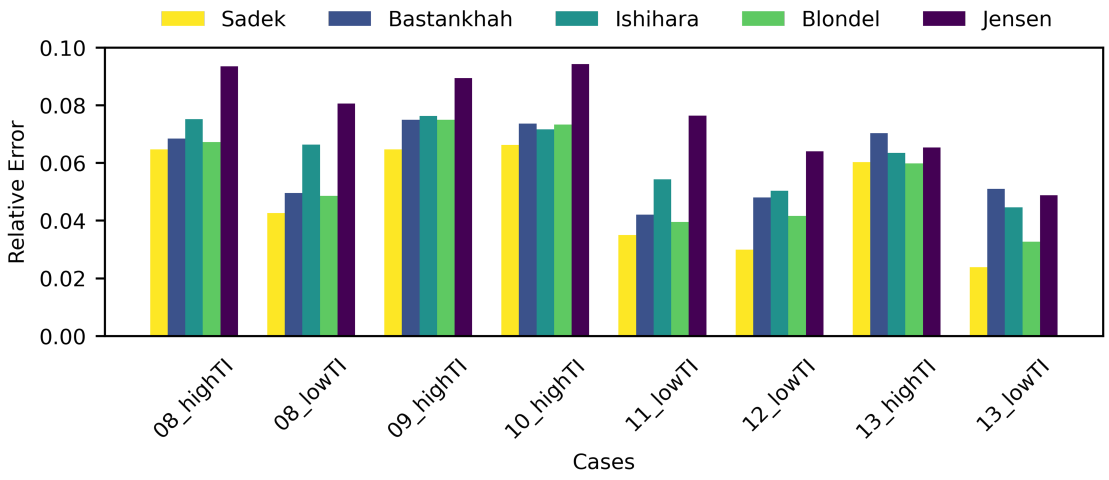

Figure 5.1: Domain-wide, L^2 norm, relative error comparing the streamwise Sadek, Bastankhah, Ishihara, Blondel, and Jensen models for each LES case in the data set.

and flexibility to a range of operating conditions. There is a shared trend to predict lower error in cases with wind speeds greater than 10 m/s. This is attributed to the fact that these models are not optimal for predicting flows below the rated operating wind speed, which for the NREL 5 MW is 11.4 m/s [22]. Ordering of errors from largest to smallest appears to be consistent for wind speeds below the rated range. The Jensen model produces the highest error while Blondel, Ishihara, and Bastankhah are comparable to one another whereas the Sadek model reports the lowest error of the group. An exception to this is the 08_lowTI case where the Ishihara model performs dissimilarly to Bastankhah and Blondel with larger error. At higher wind speeds disparities between models increases, shown in the 11_lowTI and 13_lowTI cases. In this region, there are also instances where all models are performing seemingly uniformly, as seen in the 13_highTI case. This shows the varying degrees of sensitivity to operational conditions across all models, especially

turbulence intensity as the low intensity cases display larger variations in model performance compared to the high intensity cases.

Figure 5.2 shows hub-height, horizontal contours for each model, taken from a representative case. All contours share the same color range determined by the extreme values found across all six plots. Here, the Bastankhah model is responsible for extending the color range by severely under predicting the near wake velocity. Being a far wake model, the FLORIS implementation of this work addresses the near wake with the same formulation used to describe the far wake. The behavior of these two regions are not alike and it is this repurposing of descriptions that is responsible for under predicting the near wake velocity. Further, these regions are combined with a sum of squares creating a non-physical transition between the two.

The Ishihara model is the only flow field which includes the effects induction however, the amplitude function used to include this effect distorts the downstream portion of the wake. The super-Gaussian function used by Blondel over predicts the wake width yet shows good agreement in the wake velocity. The Jensen model is the only non-Gaussian model being evaluated leading to a sharp separation between the wake and surrounding flow. Even so, this model accomplishes its target of producing a simplified wake structure, forfeiting any flexibility and detail in favor of a simplicity.

Figure 5.3 is a direct comparison between hub height contours of the SOWFA training data and corresponding Sadek model with both plots again sharing the same color range. The near wake hub jet is captured by the model with the leading turbine matching well while the wake velocity of following turbine is under predicted, obscuring the hub jet. Empirical relations do not produce an exact match for each

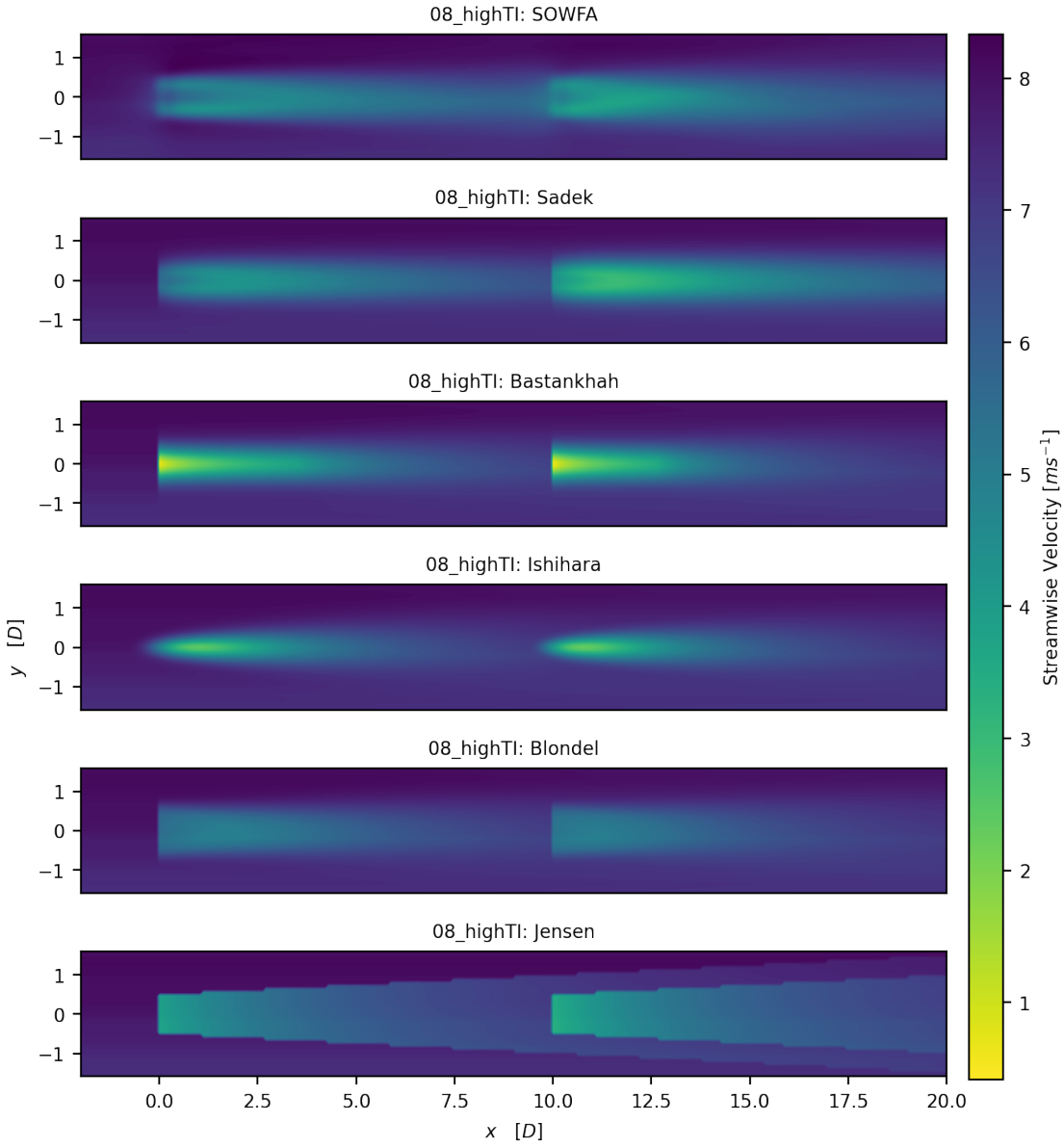

Figure 5.2: Hub height, horizontal contours of the streamwise velocity taken from the SOWFA training data, Sadek model, and existing FLORIS models for the 08_hightTI case.

case used to train them. This is causing the differences seen in wake velocity between the proposed work and reference data. Nonetheless, a domain-wide L^2 norm error

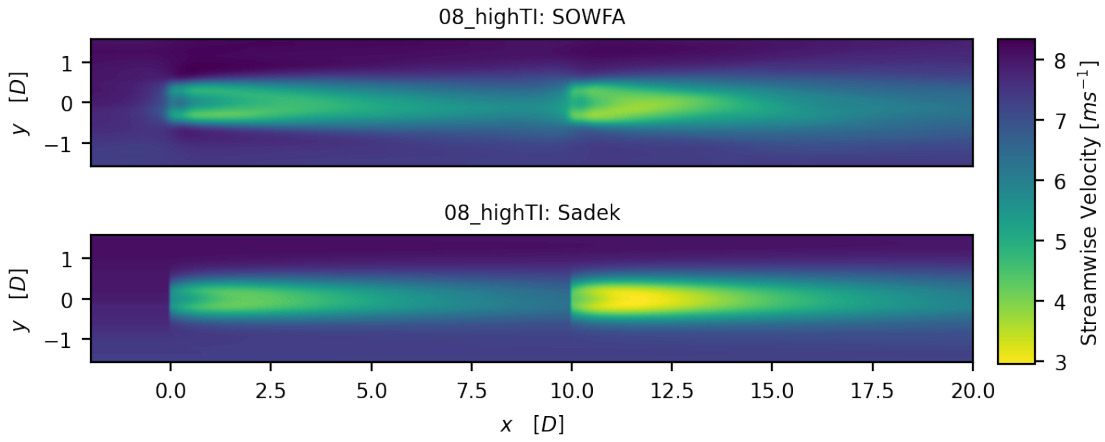

Figure 5.3: Hub height, horizontal contours of the streamwise velocity directly comparing the SOWFA training data and Sadek model for the 08_hightTI case.

of only 6.1% is computed for this case. The non-physical masking of the wake becomes evident with a sharp discontinuity appearing at the rotor plane of each turbine. Masking is done in the velocity deficit space since within the free steam it is zero. This does not affect the flow field upstream of the turbine when transformed into absolute velocities.

5.2 Spanwise Model

The King model is the only spanwise/vertical model being compared against in this analysis. Due to the magnitudes of the these flows relative error was not a suitable performance metric. Small differences between the model and training data are reported as large errors due to the magnitude of the normalizing velocity. Here, a Symmetric Mean Absolute Percentage Error (SMAPE) is introduced. This new performance metric remedies the issues found when dealing with the zero-centered spanwise and vertical velocities. Expressed as,

$$\text{SMAPE} = \frac{1}{n}\sum_{t=1}^{n}\frac{|M_t - D_t|}{|M_t| + |D_t|}, \tag{5.1}$$

n is the total number of points in the wake volume and M_t, D_t are the model and data values sampled at point n in the domain, respectively. Single vertical bars signify absolute values. Relative error values were reported over 100% for both models while SMAPE bounds this between 0% and 100%. To compare the performance of the proposed Sadek model to the King model the SMAPE is calculated for both across the training data set. Shown in Fig. 5.4 are the domain-wide SMAPE for both the Sadek and King spanwise velocity models across every case in the data set.

Even by incorporating SMAPE, it is exceptionally difficult to characterize the performance of a model with a single scalar value. Still, the Sadek model dramatically out performs the King model, averaging less than half the error for the King model. This is further demonstrated when comparing contours of the predicted

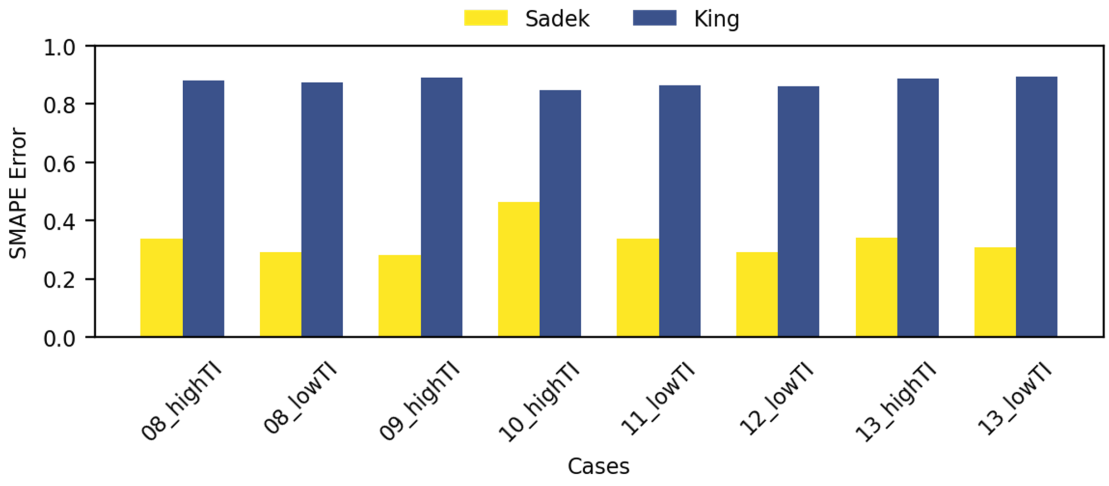

Figure 5.4: Domain-wide SMAPE comparing the spanwise Sadek and King models.

wakes generated by each model. Shown above in Fig. 5.5 are horizontal, hub-height contours of the LES data and Sadek model of the spanwise components for a representative case. The King model is not included since it does not depict any rotation and produces a zero velocity flow field in this view.

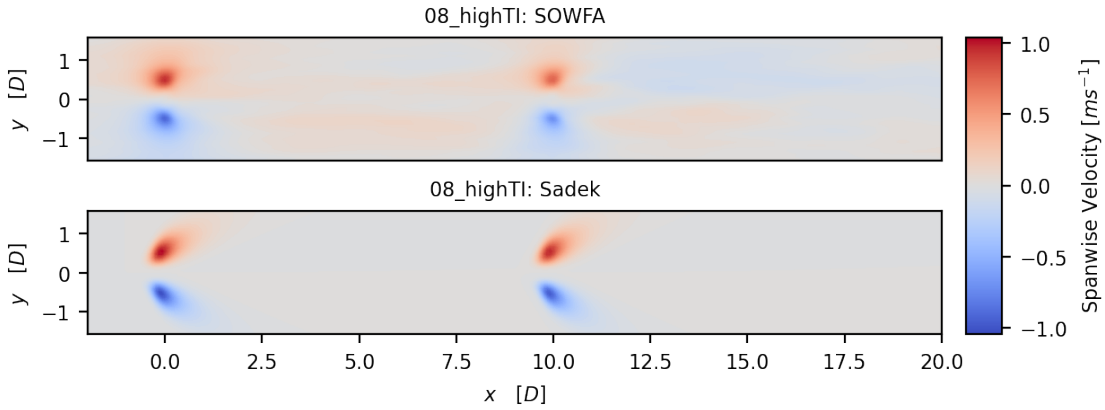

Figure 5.5: Hub height, horizontal contours of the spanwise velocity directly comparing the SOWFA training data and Sadek model for the 08_hightTI case.

Within this contour, near wake effects are shown as the two characteristic nodes reorient themselves. The Sadek model captures this properly, even describing the induction occurring upstream of the rotor. However, this effect is slightly exaggerated as it penetrates farther into the wake and over predicts the magnitude of each node compared to what is shown in the data. The depiction of these features has them expand linearly in order to align and merge with the far wake components. While not accurate to the data this implementation is done to better convey bulk rotation and is sufficient to describe the general behavior of this region. The King model does not portray this, simply arranging the two nodes in there final position from the start of the wake.

More meaningful comparisons are drawn by examining planes which reveal the

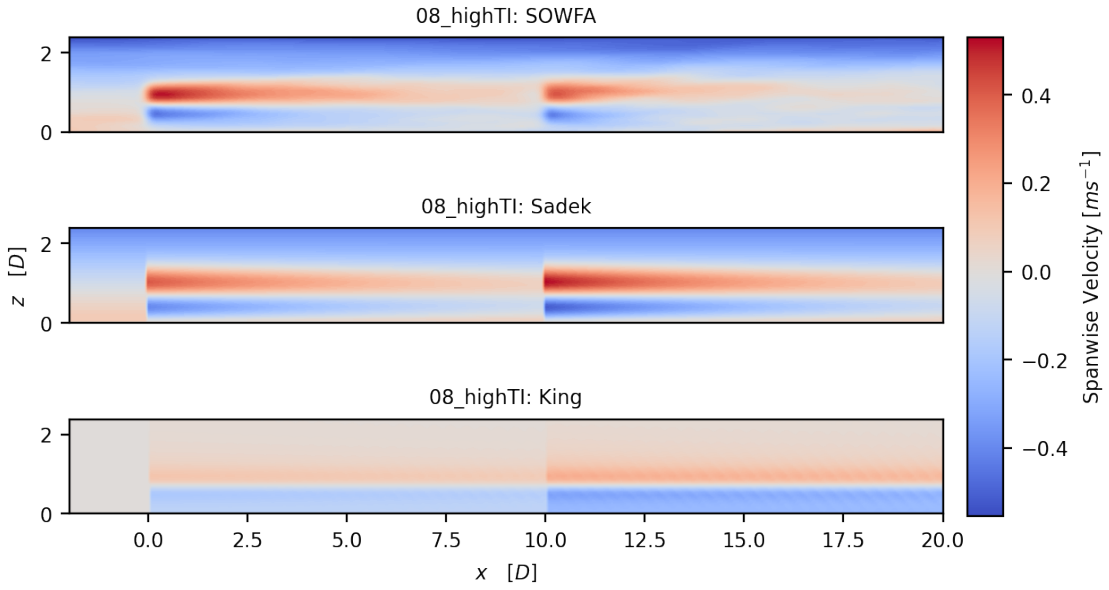

Figure 5.6: Tower centered, vertical contours of the spanwise velocity taken from the SOWFA training data, Sadek, and King models for the 08_hightTI case.

far wake behavior. Figure 5.6 shows vertical, tower-centered contours of the SOWFA training data, Sadek, and King vertical velocity models. The SOWFA data shows the trailing nodes which make up a majority of the wake structure. In application, the King model consistently under predicts the wake velocity for every case in the data set. The Sadek model includes inflow using a linear veer model expressed in Equation 2.24, seen in the background of Fig. 5.6. This matches well with the SOWFA data and contributes to the reduction in error compared to the King model which omits background flow. Not depicted by either models is the asymmetric behavior of the nodes as they decay downstream. The negative velocity distribution decays slightly faster than the positive region, highlighted by the second turbine in the SOWFA data.

5.3 Vertical Model

Repeating our analysis with the vertical velocity, the SMAPE for both the Sadek and King models is shown in Fig. 5.7.

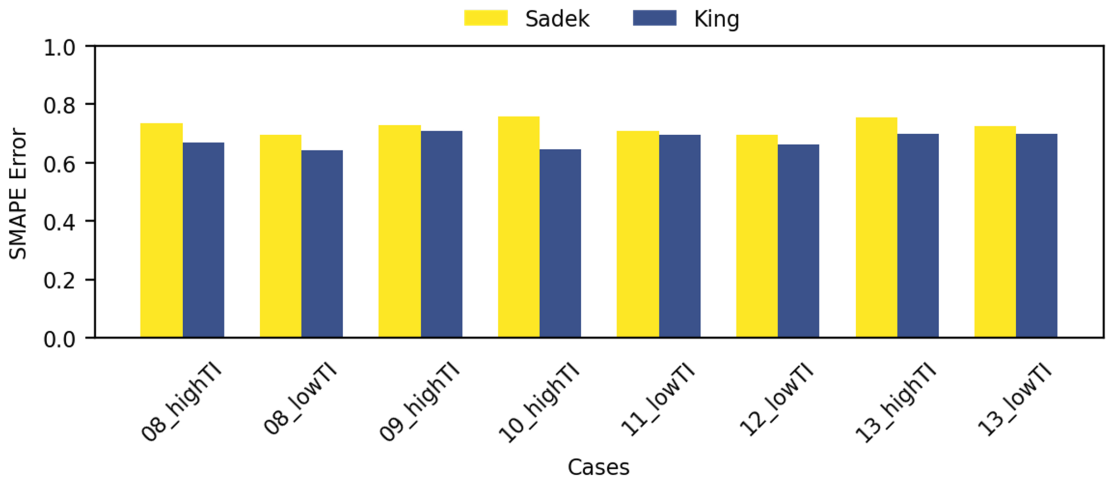

Figure 5.7: Domain-wide SMAPE comparing the vertical Sadek and King models.

The difference between these two models is minimal compared to the large disparity seen in the spanwise comparison however, both errors are exceptionally large, likely due to the magnitude of the surrounding flow in the training data. Unlike the streamwise and spanwise models, there is no prescribed inflow profile for the vertical component being set uniformly to zero velocity.

Examining the far wake behavior reveals the shortcomings of each model. Figure 5.8 shows horizontal, hub-height contours of the LES data, Sadek model, and King model of the vertical components for the same representative case. This view shows the far wake nodes decaying as they evolve downstream. The Sadek model appropriates predicts the wake velocity while the King model again is under predicting.

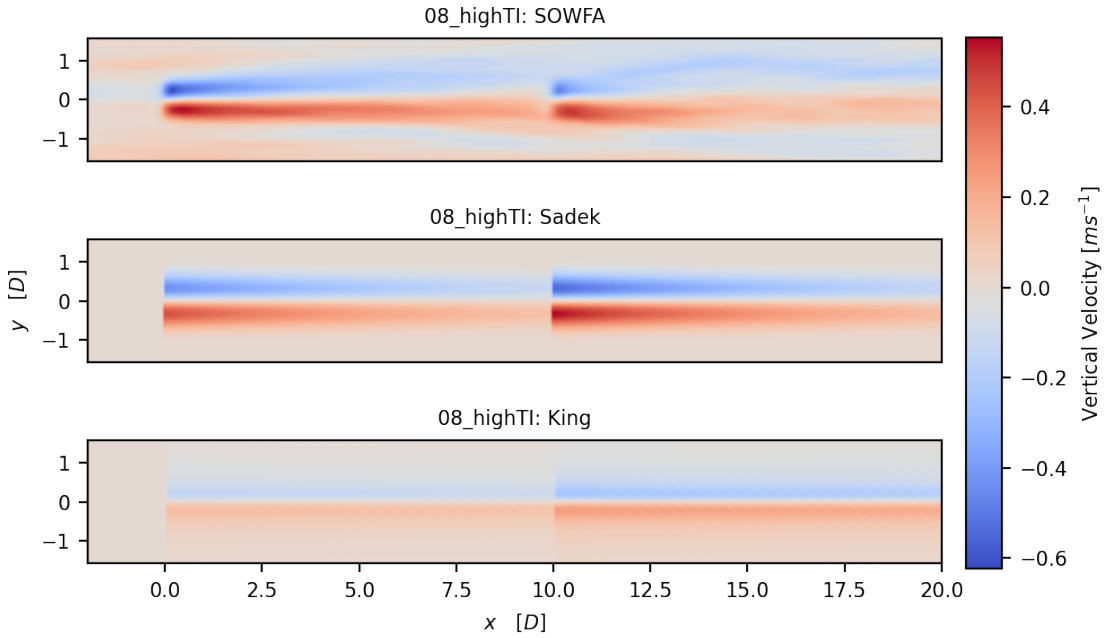

Figure 5.8: Hub height, horizontal contours of the vertical velocity taken from the SOWFA training data, Sadek, and King models for the 08_hightTI case.

Asymmetric behavior of the decay between the positive and negative velocity nodes is shown by the SOWFA data where the negative velocity distribution decays more quickly than the positive. This is highlighted by the second turbine in this array. The Sadek model does not depict this behavior as both nodes are defined to have equal and opposite amplitudes, simplifying the model.

Addressing the near wake, Fig. 5.9 shows vertical, tower-centered contours of the LES training data and Sadek vertical velocity model. This again highlights the near wake component of the Sadek model which the King model omits. Implementation of the mirror condition to create a no-slip surface is seen affecting the wake in the Sadek model. The negative velocity in the near wake is clipped by the mirror condition, preventing it from penetrating into the ground.

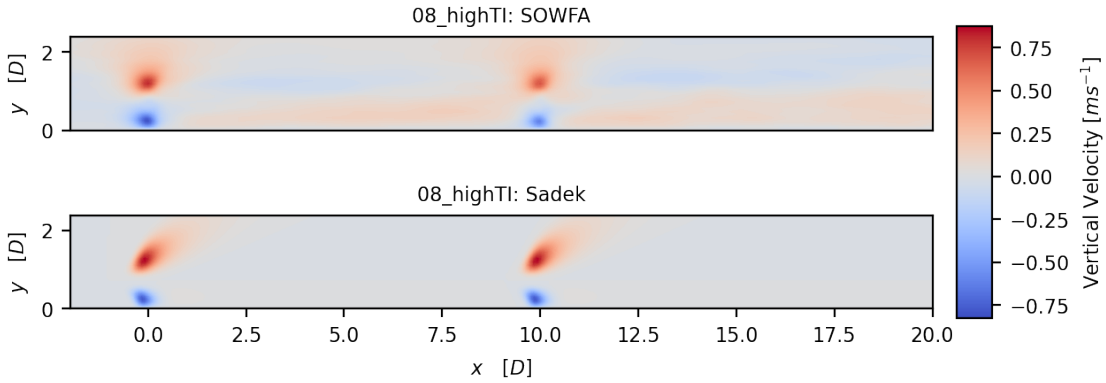

Figure 5.9: Tower centered, vertical contours of the vertical velocity directly comparing the SOWFA training data and Sadek model for the 08_hightTI case.

Mass conservation capabilities are considered by computing the residuals of the continuity equation as shown in Equation 4.5. To interpret this in a one dimensional sense each spanwise-vertical crossplane in the volume of residuals is averaged and plotted as a function of downstream position, shown in Fig. 5.10. This description of mass conservation serves as a concise way to compare all the models. The Sadek suite designed all three of its model simultaneously with the aim of mass conservation in mind. However, existing streamwise FLORIS models were not constructed with accompanying spanwise and vertical components; here the King model has become the default FLORIS spanwise/vertical surrogate and will be used to supply the spanwise and vertical components during analysis.

Figure 5.10 shows the average residuals of each spanwise-vertical plane as a function of downstream position for all models. The inset figure is a focused view of the near wake of the leading turbine to better distinguish the response of each model. Residuals from the SOWFA data serve as a baseline comparison shown in solid black. The largest residuals for all models occurs at the rotor plane of each

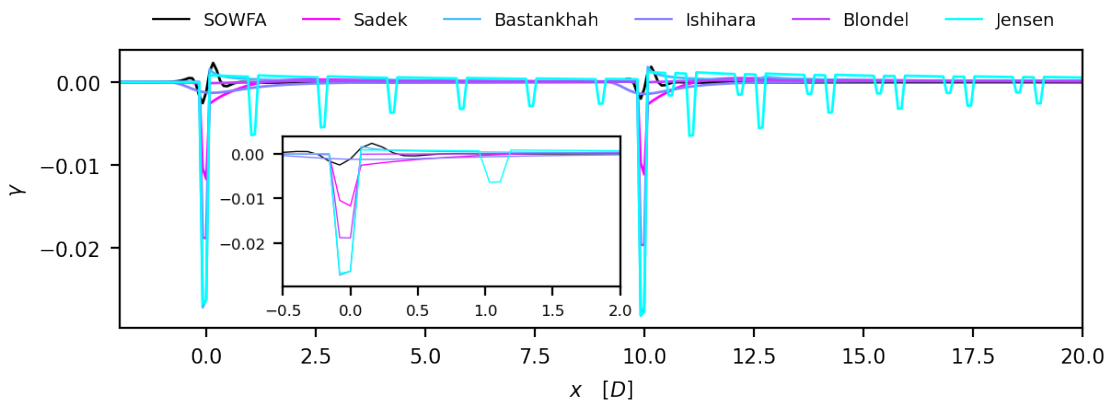

Figure 5.10: Continuity residuals averaged across each spanwise-vertical plane, plotted against normalized downstream distance for the 08_highTI case.

turbine where even in the SOWFA data there is violation of mass consistency. There are vastly different responses amongst all the models; The non-physical wake edge of the Jensen model is seen here, granted a non-physical feature is not expected to comply with conservation principles. Shown in decreasing order of residuals at either rotor plane are Jensen, Bastankhah, Blondel, Sadek, and Ishihara. Here, the Sadek model performs nominally displaying neither the highest or lowest residuals at this point. Conversely, the Ishihara model produces residuals comparable to the SOWFA data. This is surprising given that the Ishihara and King models are not designed to optimally conserve mass together.

The far wake behavior of the models converge to zero. Recovery from the initial rotor plane discontinuity to steady residuals is an additional metric to consider. Despite the large spikes seen in the Jensen model, the mean recovery after the rotor plane appears to occur quickly. Worth noting is that the growth rate of the first turbine can be seen in the second turbine's residuals in Fig. 5.10 as a series of staggered discontinuities. The Blondel model recovers immediately while the Sadek

and Bastankhah converge within the first rotor diameter downstream. Additionally, the Ishihara, Sadek, and Blondel models all appear to be nearly negative definite, while the SOWFA data, Bastankhah, and Jensen models all contain both positive and negative residual values. This is only a comparison of mass conservation and does not depict the accuracy of the models with relation to the flow field. Despite the performance seen by the paired Ishihara, King models, the individual accuracy of each component does not sufficiently recreate the flow field.

Chapter 6

Conclusion

A set of new, three-dimensional, analytical wake models is developed to better depict near wake flows for onshore, non-misaligned turbines. Conservation of mass is considered in a residual minimizing optimization process. This model improves upon existing work by better predicting the wake flows across multiple inflow conditions, demonstrated by producing the lowest relative error compared to all existing FLORIS models across the entire training data set. Preferential behavior towards wind speeds within the rated range is shown as a reduction error. Despite having better performance across each individual component, the combined mass conservation capabilities are not supreme amongst the considered models. The Sadek model did not perform in either extreme with regards to mass consistency, performing nominally amongst the considered works. Decreasing residual magnitudes at the rotor plane are found to be Jensen, Bastankhah, Blondel, Sadek, and Ishihara, respectively. The Ishihara model paired with the King model was able to better conserve mass than both the Sadek model and LES. This reveals one of the many balances which occur during wake modeling: individual component performance as against concurrent mass consistency. In the case of the Sadek model each component fairs better when compared directly to its counterparts, qualitatively. When assembled

for mass conservation this advantage disappears, performing only moderately in comparison to its counterparts; highlighting the importance of choosing the appropriate error metric depending on the application for a model. With the Sadek model being designed to better depict near wake flows the domain-wide, L^2 norm stands as a better performance metric than a one dimensional interpretation of mass conservation. In the matter of model adaptability, the streamwise Sadek model shows a high level of flexibility across all the cases, performing the best in every case. Given the scale with which wind energy operates, being able to produce increases in performance on the scale of single digit percentages translates into tremendous earnings in power production. Every gain in performance is needed to phase out fossil fuels and introduce renewables as an equivalently capable alternative. Introducing a new, low fidelity model which includes previously disregarded physics stands to advance wind energy by producing better representations of farm-wide flows during controls and performance oriented design of wind turbine arrays.

Chapter 7

Future Work

Future work includes porting the Sadek model into the latest installment of FLORIS. Joining this established, open source framework would allow anyone to use this tool, further developing and improving upon this work. Additionally, incorporating a coupled wake added turbulence (WAT) model would be beneficial given the dependence the Sadek wake model places on local turbulence intensity. Not included in this work are the effects of yaw-misalignment on wake trajectory. To maximize the utility of the Sadek model incorporating these effects is needed to expand the design opportunities available during wind plant optimization. Lastly, model validation is to be conducted using full size, field measurement. This is an excellent opportunity for this work to carry into the American wake experiment (AWAKEN) which is an international field campaign focused on studying and measuring the effects of onshore turbine generate wakes [28].

Bibliography

[1] *Renewable Power Generation Costs in 2020*, tech. rep., International Renewable Energy Agency, IRENA, Abu Dhabi, United Arab Emirates, 2020.

[2] *Global temperature*, 2021. [Online; accessed April 29, 2022].

[3] *Sea level*, 2022. [Online; accessed April 29, 2022].

[4] M. Bastankhah and F. Porté-Agel, *A new analytical model for wind-turbine wakes*, Renewable Energy, 70 (2014), pp. 116–123.

[5] C. Bay, J. R. King, P. A. Fleming, L. Martinez, R. M. Mudafort, E. J. Simley, and M. J. Lawson, *Floris: A brief tutorial*, tech. rep., National Renewable Energy Lab.(NREL), Golden, CO (United States), 2020.

[6] F. Blondel and M. Cathelain, *An alternative form of the super-gaussian wind turbine wake model*, Wind. Energy Sci. Discuss, 2020 (2020), pp. 1–16.

[7] T. Burton, N. Jenkins, D. Sharpe, and E. Bossanyi, *Wind energy handbook*, John Wiley & Sons, 2011.

[8] A. Clifton, A. Smith, and M. Fields, *Wind plant preconstruction energy estimates. current practice and opportunities*, tech. rep., National Renewable Energy Lab.(NREL), Golden, CO (United States), 2016.

[9] B. M. Doekemeijer, D. van der Hoek, and J.-W. van Wingerden, *Closed-loop model-based wind farm control using floris under time-varying inflow conditions*, Renewable Energy, 156 (2020), pp. 719–730.

[10] M. Dörenkämper, B. Witha, G. Steinfeld, D. Heinemann, and M. Kühn, *The impact of stable atmospheric boundary layers on wind-turbine wakes within offshore wind farms*, Journal of Wind Engineering and Industrial Aerodynamics, 144 (2015), pp. 146–153.

[11] C. Draxl, B. Hodge, A. Clifton, and J. McCaa, *Overview and meteorological validation of the wind integration national dataset toolkit*, tech. rep., National Renewable Energy Lab.(NREL), Golden, CO (United States), 2015.

[12] L. Fingersh, M. Hand, and A. Laxson, *Wind turbine design cost and scaling model*, tech. rep., National Renewable Energy Lab.(NREL), Golden, CO (United States), 2006.

[13] J. Fischereit, R. Brown, X. G. Larsén, J. Badger, and G. Hawkes, *Review of mesoscale wind-farm parametrizations and their applications*, Boundary-Layer Meteorology, 182 (2022), pp. 175–224.

[14] P. Fleming, P. Gebraad, J.-W. van Wingerden, S. Lee, M. Churchfield, A. Scholbrock, J. Michalakes, K. Johnson, and P. Moriarty, *Sowfa super-controller: A high-fidelity tool for evaluating wind plant control approaches*, tech. rep., National Renewable Energy Lab.(NREL), Golden, CO (United States), 2013.

[15] J. R. Garratt, *The atmospheric boundary layer*, Earth-Science Reviews, 37 (1994), pp. 89–134.

[16] P. M. Gebraad, F. Teeuwisse, J. Van Wingerden, P. A. Fleming, S. Ruben, J. Marden, and L. Pao, *Wind plant power optimization through yaw control using a parametric model for wake effects—a cfd simulation study*, Wind Energy, 19 (2016), pp. 95–114.

[17] General Electric, *Blade of glory: A critical offshore wind turbine component passes a key milestone*, 2020. [Online; accessed April 29, 2022].

[18] N. Hamilton, C. J. Bay, P. Fleming, J. King, and L. A. Martínez-Tossas, *Comparison of modular analytical wake models to the lillgrund wind plant*, Journal of Renewable and Sustainable Energy, 12 (2020), p. 053311.

[19] K. L. Horgan, D. M. Schultz, J. E. Hales Jr, S. F. Corfidi, and R. H. Johns, *A five-year climatology of elevated severe convective storms in the united states east of the rocky mountains*, Weather and Forecasting, 22 (2007), pp. 1031–1044.

[20] T. Ishihara and G.-W. Qian, *A new gaussian-based analytical wake model for wind turbines considering ambient turbulence intensities and thrust coefficient effects*, Journal of Wind Engineering and Industrial Aerodynamics, 177 (2018), pp. 275–292.

[21] N. O. Jensen, *A note on wind generator interaction*, (1983).

[22] J. Jonkman, S. Butterfield, W. Musial, and G. Scott, *Definition of a 5-mw reference wind turbine for offshore system development*, tech. rep., National Renewable Energy Lab.(NREL), Golden, CO (United States), 2009.

[23] A. Keane, *Advancement of an analytical double-gaussian full wind turbine wake model*, Renewable Energy, 171 (2021), pp. 687–708.

[24] J. King, P. Fleming, R. King, L. A. Martínez-Tossas, C. J. Bay, R. Mudafort, and E. Simley, *Control-oriented model for secondary effects of wake steering*, Wind Energy Science, 6 (2021), pp. 701–714.

[25] J. C. Lee and M. J. Fields, *An overview of wind-energy-production prediction bias, losses, and uncertainties*, Wind Energy Science, 6 (2021), pp. 311–365.

[26] L. A. Martínez-Tossas, J. Annoni, P. A. Fleming, and M. J. Churchfield, *The aerodynamics of the curled wake: A simplified model in view of flow control*, Wind Energy Science (Online), 4 (2019).

[27] L. Mishnaevsky, K. Branner, H. N. Petersen, J. Beauson, M. McGugan, and B. F. Sørensen, *Materials for wind turbine blades: an overview*, Materials, 10 (2017), p. 1285.

[28] P. Moriarty, N. Hamilton, M. Debnath, T. Herges, B. Isom, J. K. Lundquist, D. Maniaci, B. Naughton, R. Pauly, J. Roadman, et al., *American wake experiment (awaken)*, tech. rep., Lawrence Livermore National Lab.(LLNL), Livermore, CA (United States ..., 2020.

[29] F. Mühle, M. S. Adaramola, and L. Sretran, *The effect of the number of blades on wind turbine wake-a comparison between 2-and 3-bladed rotors*, in Journal of Physics: Conference Series, vol. 753, IOP Publishing, 2016, p. 032017.

[30] M. Nakhchi, S. W. Naung, and M. Rahmati, *High-resolution direct numerical simulations of flow structure and aerodynamic performance of wind turbine airfoil at wide range of reynolds numbers*, Energy, 225 (2021), p. 120261.

[31] A. Niayifar and F. Porté-Agel, *Analytical modeling of wind farms: A new approach for power prediction, energies, 9, 741*, 2016.

[32] J. Nocedal and S. J. Wright, *Conjugate gradient methods*, Numerical optimization, (2006), pp. 101–134.

[33] NREL, *Floris. version 2.4*, 2021.

[34] A. Olabi and M. A. Abdelkareem, *Renewable energy and climate change*, Renewable and Sustainable Energy Reviews, 158 (2022), p. 112111.

[35] P. J. Schubel and R. J. Crossley, *Wind turbine blade design*, Energies, 5 (2012), pp. 3425–3449.

[36] R. Shakoor, M. Y. Hassan, A. Raheem, and Y.-K. Wu, *Wake effect modeling: A review of wind farm layout optimization using jensen[U+05F3] s model*, Renewable and Sustainable Energy Reviews, 58 (2016), pp. 1048–1059.

[37] Q. M. Soesanto, T. Yoshinaga, and A. Iida, *Anisotropic double-gaussian analytical wake model for an isolated horizontal-axis wind turbine*, Energy Science & Engineering, (2022).

[38] G. Spagnuolo, G. Petrone, S. V. Araujo, C. Cecati, E. Friis-Madsen, E. Gubia, D. Hissel, M. Jasinski, W. Knapp, M. Liserre, et al., *Renewable energy operation and conversion schemes: A summary of discussions during the seminar on renewable energy systems*, IEEE Industrial Electronics Magazine, 4 (2010), pp. 38–51.

[39] TLPOSCHARSKY, *Wind turbine at dusk*, 2010. [Online; accessed April 29, 2022].

[40] Vatenfall, *Horns rev offshore wind farm*, 2010. [Online; accessed April 29, 2022].

[41] L. Vermeer, J. N. Sørensen, and A. Crespo, *Wind turbine wake aerodynamics*, Progress in aerospace sciences, 39 (2003), pp. 467–510.

[42] Wikimedia, *File:iss-40 thunderheads near borneo*, 2015. [Online; accessed April 29, 2022].

[43] R. H. Wiser, M. Bolinger, B. Hoen, D. Millstein, J. Rand, G. L. Barbose, N. R. Darghouth, W. Gorman, S. Jeong, A. D. Mills, et al., *Land-based wind market report: 2021 edition*, tech. rep., Lawrence Berkeley National Lab.(LBNL), Berkeley, CA (United States), 2021.

[44] W. Zhang, C. D. Markfort, and F. Porté-Agel, *Near-wake flow structure downwind of a wind turbine in a turbulent boundary layer*, Experiments in fluids, 52 (2012), pp. 1219–1235.

Appendix A

Empirical Values

A.1 parameter values

All parameters follow the generic form,

$$\kappa = C_0 Ti^{C_1} {C_t}^{C_2} \tag{1.1}$$

Parameter	C_0	C_1	C_2
a_{MW}	7.93×10^{-1}	-4.97×10^{-2}	-5.00×10^{-1}
b_{MW}	2.83×10^{-1}	4.58×10^{-1}	-8.27×10^{-1}
c_{MW}	1.23	4.10×10^{-1}	-1.94×10^{-1}
k_{MW}	1.57×10^{-2}	1.53×10^{-2}	NA
$\varepsilon_{\mathrm{MW}}$	3.22×10^{-1}	0	0
a_{HJ}	2.71×10^{-1}	-4.06×10^{-1}	5.28×10^{-1}
b_{HJ}	2.06	4.74×10^{-1}	-1.73
c_{HJ}	2.23	1.98×10^{-1}	-1.18
$\varepsilon_{\mathrm{HJ}}$	1.5×10^{-1}	0	0
a_{TA}	2.58×10^{-2}	-4.07×10^{-1}	1.91
b_{TA}	7.91	9.30×10^{-1}	-9.68×10^{-1}

Table A.1: Streamwise velocity deficit model empirical constants

Parameter	C_0	C_1	C_2
$a_{v,\text{near}}$	112.2	6.90×10^{-1}	13.2
$b_{v,\text{near}}$	21.4	5.84×10^{-2}	-3.83×10^{-1}
$c_{v,\text{near}}$	6.05	3.42×10^{-3}	-2.67×10^{-1}
$\alpha_{v,\text{near}}$	3.43×10^{-1}	1.71×10^{-1}	-3.62×10^{-1}
$\mu_{v,\text{near}}$	3.47×10^{-1}	0	1.88×10^{-1}
$C_{v,\text{far}}$	5.06×10^{-1}	-6.47×10^{-2}	-6.72×10^{-2}
$\beta_{v,\text{far}}$	1.73×10^{-1}	1.23×10^{-1}	0
$\mu_{v,\text{far}}$	3.46×10^{-1}	0	4.87×10^{-1}

Table A.2: Spanwise velocity model empirical constants

Parameter	C_0	C_1	C_2
$a_{w,\text{near}}$	4.12×10^{-2}	-2.02×10^{-1}	-4.33
$b_{w,\text{near}}$	26.79	-1.16×10^{-2}	5.98×10^{-1}
$c_{w,\text{near}}$	9.46	-3.10×10^{-2}	1.18
$\alpha_{w,\text{near}}$	3.34×10^{-1}	-9.25×10^{-3}	3.11×10^{-1}
$\mu_{w,\text{near}}$	3.29×10^{-1}	-6.91×10^{-3}	5.39×10^{-2}
$C_{w,\text{far}}$	4.34×10^{-1}	-6.65×10^{-2}	-1.68×10^{-1}
$\beta_{w,\text{far}}$	1.77×10^{-1}	1.31×10^{-1}	4.35×10^{-3}
$\mu_{w,\text{far}}$	3.11×10^{-1}	-4.70×10^{-4}	3.31×10^{-1}

Table A.3: Vertical velocity model empirical constants